Plasma Sources
Science and
Technology

PAPER • **OPEN ACCESS**

Sub-1 V/cm E-FISH-based picosecond electric field measurements in atmospheric pressure air

To cite this article: Grayson LaCombe *et al* 2025 *Plasma Sources Sci. Technol.* **34** 025001

OPEN ACCESS
IOP Publishing
Plasma Sources Science and Technology
Plasma Sources Sci. Technol. **34** (2025) 025001 (11pp)
https://doi.org/10.1088/1361-6595/adae32

Sub-1 V/cm E-FISH-based picosecond electric field measurements in atmospheric pressure air

Grayson LaCombe[1], Jianan Wang[1], Kraig Frederickson[2] and Marien Simeni Simeni[1,*]

[1] Department of Mechanical Engineering, University of Minnesota, 111 Church St SE, Minneapolis, MN 55455, United States of America
[2] Naval Undersea Warfare Center, Division Keyport, 610 Dowell St, Keyport, WA 98345, United States of America

E-mail: msimenis@umn.edu

Received 5 October 2024, revised 7 January 2025
Accepted for publication 24 January 2025
Published 7 February 2025

Abstract

We report on the development of a highly sensitive electric field induced second harmonic generation diagnostic setup capable of measuring electric field strengths as low as 1 V cm^{-1} at the picosecond time scale under atmospheric pressure conditions. This unprecedented sensitivity is achieved through passive homodyne detection, which utilizes stray signals generated by an optical component in the beam path. Our detection limit of 0.3–0.5 V cm^{-1} represents an improvement of over 2–3 orders of magnitude compared to previous reports (100–1000 V cm^{-1}) in the literature. Additionally, we demonstrate sensitivity to the polarity of the electric field. Experimental results are corroborated by simulations of the 400 ps time-resolved homodyne process, offering deeper insights into the enhanced detection capabilities and the system's ability to resolve the field sign.

Keywords: E-FISH, electric field, atmospheric pressure, picosecond time-resolved, homodyne detection, Sub-1 V cm^{-1}

1. Introduction

In electrical gas discharges, the input electrical energy is preferentially transferred to kinetic energy of free electrons. This preference arises from the significantly lower mass of electrons compared to other gas particles. In detail, free electrons gain kinetic energy when accelerated by an externally applied electric field typically resulting from an applied voltage difference on a pair of metal electrodes. Electrons subsequently generate a complex chemistry by transferring a portion of their energy through collisions with the surrounding gas particles. Phenomena such as gas heating, rotational excitation of molecules within the gas, vibrational excitation of those molecules, electronic excitation of both atomic and molecular species, as well as dissociation and ionization all occur as consequences of these collisional energy transfers initiated by electrons. As highlighted in the 2022 Plasma Roadmap, the field of Low-Temperature Plasma science and technology heavily relies on our capability to harness, engineer, and control these complex energy transfers toward very diverse applications [1].

A crucial parameter influencing the aforementioned energy transfers and electron kinetics is the reduced electric field, denoted as E/N, where E represents the magnitude of the electric field within the plasma and N is the total gas number density. This parameter intuitively accounts for scaling the

* Author to whom any correspondence should be addressed.

effects of accelerating electric fields by the number density of the available collisional partners [2]. The accurate measurement of the electric field magnitude, particularly in high-pressure conditions, becomes imperative due to the exponential dependence of rate coefficients for electron impact-driven processes on *E/N* [3, 4]. Furthermore, sub-nanosecond resolved E-field magnitude measurements are often needed under high-pressure conditions because of the very transient electric field dynamics when plasmas are generated using excitation voltages featuring fast nanosecond rise times [5].

The electric field induced second harmonic (E-FISH) generation diagnostic [6] has recently gained a lot of attention for electric field measurements in high-pressure electrical discharges. The impressive potential of this technique was put on full display through the large variety of measurements. We can list for instance measurements in plasma-enhanced flames [7–9], in plasma jets [10–12], in volumetric ionization waves [13–18], in corona discharges [19–21] and in surface ionization waves [22, 23]. Very recent works related to this technique have focused either on the understanding of the fundamental question of the coherent growth of the signal under tight focusing conditions [24], on leveraging pulse-burst lasers to achieve single acquisition measurements [25] or on improving the spatial resolution of this diagnostic along the laser beam path [26–28]. Interestingly, regarding the latter aspect, research groups at Ohio State University and Sandia National Laboratories have reported a factor of 2 increase of the spatial resolution in the propagation direction of the laser beam to about 500 μm when deploying a 1° crossed-probe beam strategy [26, 27]. However, this gain came with the drawback of a decrease in the measured signal by over two orders of magnitude. Achieving a micrometer spatial resolution is key when probing high-pressure filamentary discharges featuring typical diameters around 50–100 μm.

In this context, we report on the development of a very sensitive E-FISH generation diagnostic setup. This system is capable of measuring electric field magnitudes as low as 1 $\mathrm{V\,cm^{-1}}$ in room air and at the sub-nanosecond timescale. This advancement represents an improvement by over two orders of magnitude compared to most E-FISH systems encountered in the literature, where reported detection limits are typically around 100 $\mathrm{V\,cm^{-1}}$ – 1 $\mathrm{kV\,cm^{-1}}$ [6, 22]. This enhanced capability is especially important when characterizing electric field reversals in plasma discharges [29, 30]. Accurately characterizing electric field reversals requires an E-FISH diagnostic capable of measuring low-magnitude electric fields while also being sensitive to the E-field polarity. However, the standard E-FISH approach cannot meet this polarity sensitivity requirement, as the measured signal is proportional to the square of the electric field [6]. Beyond electric field reversals, the ability to measure low-magnitude electric fields is critical for understanding numerous key phenomena across plasma physics. These include: (1) surface charges decay on dielectric surfaces in the afterglow of low to high pressure discharges [29]; (2) space charge dynamics in the afterglow of low to high pressure discharges, especially in inert gases [31]; (3) electron energy partition in atmospheric pressure discharges under low *E/N* conditions [3, 30]; (4) trapped charged-particles dynamics in the sheath of low to intermediate pressure dusty plasmas [32]; (5) charged-species dynamics in Hall-effect thrusters [33]; (6) physics of electrical double layers [34]; (7) edge localized modes at the periphery of tokamak plasmas [35]; and (8) ion–ion plasmas in electronegative gases [36]. Through a comparative analysis with standard E-FISH systems, we examine necessary upgrades and propose pathways for further development.

2. Experimental setup

Figure 1 depicts a schematic of the experimental setup. The vertically-polarized fundamental output of a mode-locked, diode-pumped picosecond Nd:YAG laser (EKSPLA, PL2231-50, 30 ps, 30 mJ maximum output at 1064 nm) operating at 50 Hz is focused between a pair of parallel plate copper electrodes using 45° incidence angle silver-protected mirrors (ThorLabs, PF10-03-P01) and an AR-coated 1 m focal length BK-7 focusing lens (Lambda Research Optics, VAR2-PCX-25.4B-1000-1064). Two colored-glass long-pass filters (ThorLabs, FGL850M, with a cut-on wavelength of 850 nm) are used to filter out any stray SH signal emanating from the interaction of the picosecond laser beam with the silver mirror surfaces as well as with the focusing lens (‘Lens 1’). The copper electrodes are identical and separated by an adjustable gap distance. These electrodes can be powered by a DC high-voltage power supply (Spellman, SL10PN150) or by the voltage output of a digital delay generator (Stanford Research Systems, DG645). Following the approach pioneered by Chng *et al* [24], we use triangular-shaped electrodes such that we can vary the effective length of the interaction region between the focused Gaussian laser beam and the region of space where the E-field is applied. Although the optimum electrode length could be directly derived from the knowledge of the Rayleigh range of the Gaussian beam, placing the triangular-shaped electrode assembly on a 3-axis translational stage allows for better control over the strength of the generated second harmonic signal. Throughout the manuscript we used an electrode length of 3.5 cm, which was found to be optimized based on E-FISH signal intensity testing. Because of the interaction between the 1064 nm beam and the DC-applied electric field, a co-propagating E-FISH signal at 532 nm is generated. A Nd:YAG laser harmonic separator dichroic mirror (Lambda Research Optics, HHS-2506U-R532/T1064-45) reflecting 532 nm and transmitting 1064 nm is placed downstream of the electrode assembly. This results in a significant reduction of the 1064 nm beam intensity. A 1 ns rise time silicon photodiode (ThorLabs, DET10A2) is placed in the transmitted direction after the dichroic mirror. This photodiode is used for monitoring the pulse-to-pulse fluctuations of the incident 1064 nm beam intensity and for timing purposes. The photodiode is preceded by a neutral density filter

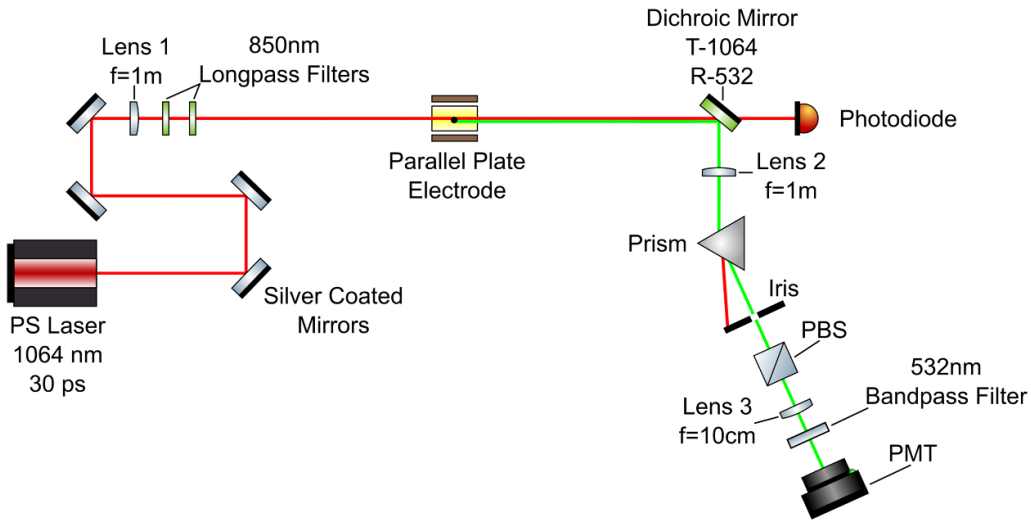

Figure 1. Schematic of the E-FISH experimental setup. The different voltage power supplies are not shown. The electrodes are 3.5 cm long along the laser beam propagation direction.

wheel to avoid saturation effects. Next, a 1 inch diameter AR-coated, 100 cm focal length lens (Lambda Research Optics, VAR2-PCX-25.4B-1000-532) collimates both the E-FISH signal at 532 nm and the remnant 1064 nm beam. A 2.5 cm CaF_2 equilateral dispersion prism (Thorlabs, PS863) then spatially separated the two different wavelengths. A polarizing cube beamsplitter (Lambda Research Optics, BPB-25.4SF2-550) is then employed to only select for vertically polarized light. A 10 cm focal length AR-coated N-BK7 plano-convex lens (Thorlabs, LA1509-A) is then leveraged to focus the E-FISH signal onto the active area of a very sensitive photomultiplier tube (PMT) at 532 nm (Hamamatsu, H7422PA-40). This PMT is powered by a dedicated low-noise power supply (Hamamatsu, C8137-02), and the signal from the PMT is amplified through a pre-amplifier (Hamamatsu, C11184). Note that the PMT is preceded by a hard-coated bandpass filter (center: 532 nm, width: 10 nm, ThorLabs, FLH532-10). The E-FISH, photodiode, and voltage waveforms are monitored using a 1 GHz bandwidth, 5 GSa/s sampling rate digital oscilloscope (LeCroy, WaveSufer4101HD).

A key aspect of this new setup resides in the removal of the monochromator, which usually precedes the PMT. We found that removing the monochromator significantly increases the E-FISH signal. However, following this removal, the system becomes very sensitive to stray light. This issue was resolved using multiple irises as well as beam tubes in the beam path. Another essential aspect of this setup is the use of a very sensitive PMT, featuring the highest efficiency at 532 nm, among the commercially available devices. Next, the optimization of the electrode length and finally the use of a diode-pumped laser featuring a superior beam spatial profile compared to flashlamp-pumped lasers.

3. Results

Figure 2 displays averaged E-FISH waveforms taken in room air for sub-breakdown DC electric fields ranging from -30 $\mathrm{V\,cm^{-1}}$ to 19 $\mathrm{V\,cm^{-1}}$ between two parallel electrodes with a gap distance of 1 cm. The laser pulse energy was fixed at 5 mJ. Throughout this manuscript, the magnitude of the Laplacian electric field at the center of the electrode gap is approximated by the value given by the ratio of the applied voltage to the gap distance. A negative DC power supply (Stanford Research Systems, PS370) is used to provide a constant low negative voltage, which is measured by a voltage probe (Teledyne Lecroy, PP026). The negative DC was initially connected to the top electrode, while the bottom electrode was grounded. In this configuration, the electric field vector pointing 'up', is defined as a 'positive' E-field (see figure 2(c)). Conversely, grounding the top electrode and connecting the bottom electrode to the negative DC power supply results in an electric field vector pointing 'down' and hence defined as a 'negative' E-field (see figure 2(f)). The PMT is operated with a control voltage (to realize the gain) of 0.725 V (corresponding to a gain value of about 5×10^5) for the positive E-field experiments, while a control voltage of 0.850 V (corresponding to a gain value of about 1.5×10^6) is leveraged for the negative E-field measurements. Figures 2(a) and (d) show the averaged PMT traces for positive and negative E-Fields respectively, while figures 2(b) and (e) show the amplitude change (compared to the 0 $\mathrm{V\,cm^{-1}}$ case) in the PMT waveform caused by the corresponding applied electric field. Each PMT trace represents an average of at least 27 000 laser shots due to the weak nature of the signal. It is important to emphasize that this large number of laser shots does not constitute a limitation to

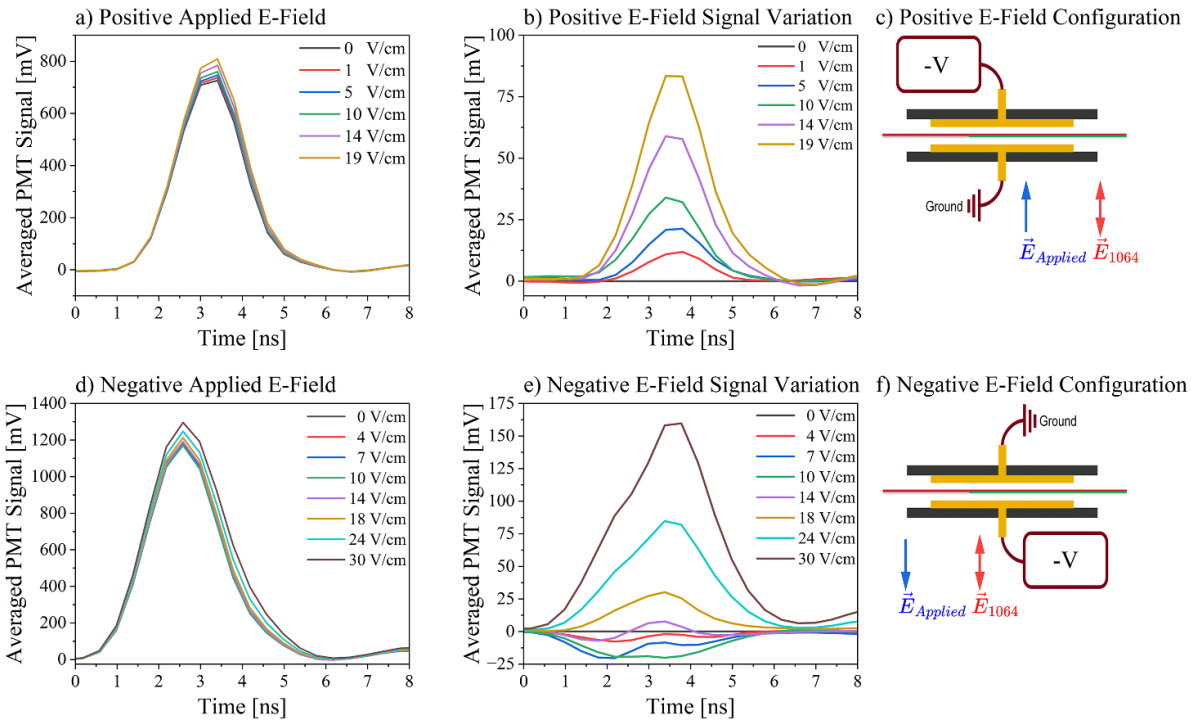

Figure 2. PMT waveforms from 27 000 laser shots averaged E-FISH tests using a 1 cm electrode gap and 5 mJ laser pulse energy. (a) PMT waveforms taken with DC-applied voltages ranging from 0 to −19 V to the top electrode resulting in a positive electric field. (b) PMT waveforms from (a) with the 0 V cm^{-1} background signal subtracted highlighting the increase in signal from the applied electric field. (c) Diagram of the electrode set up for positive electric fields. (d) PMT waveforms taken with DC-applied voltages ranging from 0 to −30 V to the bottom electrode resulting in a negative electric field. (e) PMT waveforms from (c) with the 0 V cm^{-1} background signal subtracted highlighting the change in signal from the applied electric field. (f) Diagram of the electrode set up for negative electric fields.

the applicability of this approach to laboratory plasma experiments, which typically involve experimental drifts over long periods of time due to changes in ambient temperature and pressure. Indeed, leveraging MHz repetition rate femtosecond lasers would address and resolve such challenges [37]. As depicted in figures 2(a) and (d), for both positive and negative electrode configurations, a background signal is measured in the absence of an applied E-field. From figure 2(b), when a positive E-Field is applied, the signal increases with increasing electric field from a peak (background removed) signal of 0 mV at 0 V cm^{-1} to about 83 mV at 19 V cm^{-1}. But we see a large difference even between 0 V cm^{-1} (0 mV peak) and 1 V cm^{-1} (12 mV peak), which is the same increase in PMT output voltage seen at 3 kV cm^{-1} in some of the previous studies in the literature [22]. Such a noticeable difference (0 mV vs 12 mV) readily suggests that our system is capable of measuring sub-1 V cm^{-1} DC E-fields. In fact, we expect to be able to measure positive DC E-fields down to 0.3−0.5 V cm^{-1}. It is important to point out that the ≈ 700 mV 'offset' signal measured at 0 V cm^{-1} (see figure 2(a)) is due to stray second harmonic generation (SHG) signal generated at the surface of the dichroic mirror. For negative E-fields, the signal offset at 0 V cm^{-1} (see figure 2(d)) is stronger due to the higher PMT gain used. Surprisingly, for negative E-fields, figure 2(e) evidences there is initially a decrease of the signal for applied E-field magnitudes ranging from 0 to 10 V cm^{-1} (signal decrease from 0 mV to −20 mV). Subsequently, the signal begins to rise quickly from 10 to 30 V cm^{-1} E-fields, corresponding to an increase in peak signal from −20 mV to 160 mV. Although the variation in peak PMT voltage allowed us to showcase the detection limit of our system, these signals do not clarify the relationship between measured E-FISH signals and applied voltages.

By time-integrating PMT traces in figures 2(a) and (d), we obtained the results depicted in figure 3. The latter figure corresponds essentially to typical E-FISH calibration plots relating electric field strengths to measured E-FISH signal intensities. Error bars in figure 3 correspond to 95% confidence intervals evaluated from statistical calculations over the large number of laser shots collected for each field magnitude. The positive and negative E-fields trends evidenced in figure 2 are consistently observed in figure 3. For the positive E-field case (figure 3(b)), the collected signal increases with the increase of the magnitude of the electric field at the center of the electrode gap while a more complex trend is observed for the negative E-field cases (figure 3(a)). From figure 3, for both positive and negative E-field cases, the relationship between the applied E-Field at the center of the gap and the corresponding measured E-FISH signal intensity does not follow the expected quadratic dependence ($I_{\text{meas}} \propto |\mathbf{E}_{\text{appl}}|^2$). This is especially apparent

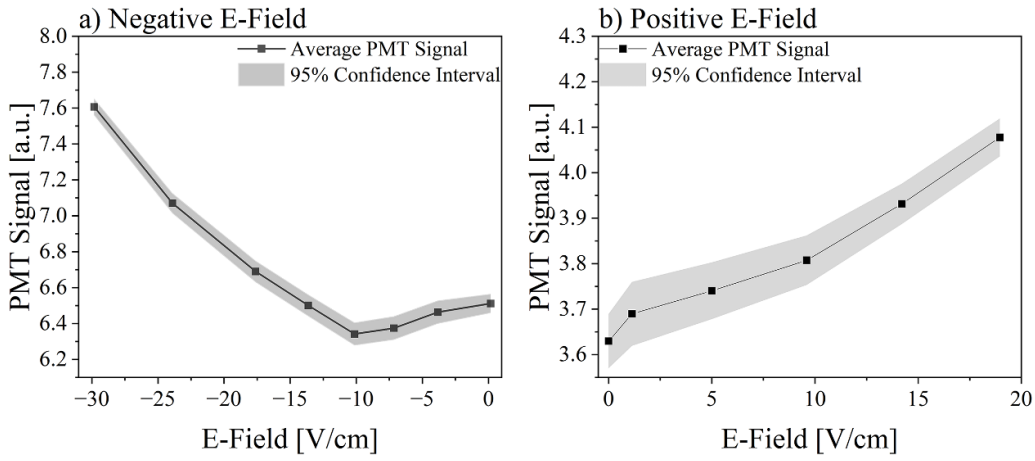

Figure 3. Time-integrated DC E-FISH signals for different applied E-Fields. The electrode gap distance is 10 mm with a width of 35.3 mm. (a) Negative electric fields. (b) Positive electric fieds.

for the negative E-Field cases (figure 3(a)), for which the E-FISH signal decays from 0 to $-10\ \mathrm{V\,cm^{-1}}$ and then increases from -10 to $-30\ \mathrm{V\,cm^{-1}}$. This unexpected trend calls for a more in-depth investigation.

To address these unexpected results, a transient low-voltage waveform featuring polarity-switching is applied to the electrode assembly. An arbitrary function generator (Tektronix, AFG1062) is used to produce a sine wave with a frequency of 10 MHz (100 ns temporal period) and an amplitude from -10.5 V to $+10.5$ V. The output of the arbitrary function generator is connected to the 'top' electrode while the bottom electrode is grounded. The electrode gap distance was 3 mm leading to an applied sub-breakdown electric field between -35 and 35 $\mathrm{V\,cm^{-1}}$. A fixed PMT control voltage of 0.850 V was employed (corresponding to a gain value of about 1.5×10^6). The time-resolved E-Fields and corresponding time-integrated PMT signals for a single voltage period are shown in figure 4(a). For this experiment, the temporal jitter of the incident laser pulse with respect to the applied voltage was 'artificially' increased by realizing a constant temporal drift of the laser pulse with respect to the AC waveform. Subsequently, for each laser shot, the photodiode, PMT, and voltage probe signals were recorded by the digital oscilloscope and placed into time bins (see [5] for more details about this procedure). Note that the segmented memory acquisition mode ('sequence' mode) of the oscilloscope was leveraged for this operation. Time bins of 400 ps were leveraged for this measurement and about 3000 laser shots were collected per bin. Remarkably, from figure 4(b), the temporal dynamics of the measured square root of the time-integrated PMT signal do not follow that of the applied E-field waveform. This comes as a surprise as the latter feature ($\sqrt{I_{\mathrm{meas}}} \propto |\mathbf{E}_{\mathrm{appl}}|$) is often leveraged for absolute calibration of transient electric field measurements in electrical discharges (see for instance [7, 8] for the case of AC excitation waveforms). Using the time-resolved data to plot a 'calibration-like' plot featuring time-integrated PMT signal vs electric field at the center of the gap, yields figure 5. The depicted trends from figure 5 are consistent with those from figure 3, with again a decrease of the measured signal between -35 and $-10\ \mathrm{V\,cm^{-1}}$ and then a subsequent increase from -10 to 35 $\mathrm{V\,cm^{-1}}$. Based on the 'basic' E-FISH paradigm ($I_{\mathrm{meas}} \propto |\mathbf{E}_{\mathrm{appl}}|^2$), one would expect figure 5 to be a parabola showcasing no offset (measured signal should be 0 for a 0 $\mathrm{V\,cm^{-1}}$ applied electric field) and the line of equation E-field = 0 should be an axis of symmetry.

4. Discussion

We hypothesize that understanding the intensity offset as well as the asymmetry of the plot displayed in figure 5 could be achieved when developing a formalism factoring in the background second harmonic signal generated by the surface of the dichroic mirror. Because the surface SHG signal generated on the dichroic mirror is a coherent beam, it also propagates to the PMT detector. The decrease of the PMT signal at negative applied voltages suggests the contribution of that stray signal to the overall PMT-measured intensity through an interference-like interaction. In the following, we assume that the stray signal from the dichroic mirror acts as a local oscillator (LO), interfering with the 'regular' E-FISH signal produced at the electrode assembly. Such an effect has been previously reported in the literature [37–39]. Interestingly, the same phenomena were also recently observed in some E-FISH experiments but were regarded as undesirable parasitic effects and subsequently mitigated [30, 40]. Using the complex field notation, we can therefore write:

$$I_{\mathrm{meas}} \propto |\overline{\mathbf{E}}_{\mathrm{total}}|^2, \tag{1}$$

where the total complex electric field $\overline{\mathbf{E}}_{\mathrm{total}}$ at 2ω (532 nm) is the sum of the electric fields emanating from the surface ($\overline{\mathbf{E}}_{2\omega}^{\mathrm{LO}}$) and E-FISH ($\overline{\mathbf{E}}_{2\omega}^{\mathrm{E-FISH}}$) processes, respectively:

$$\overline{\mathbf{E}}_{\mathrm{total}} = \overline{\mathbf{E}}_{2\omega}^{\mathrm{E-FISH}} + \overline{\mathbf{E}}_{2\omega}^{\mathrm{LO}}, \tag{2}$$

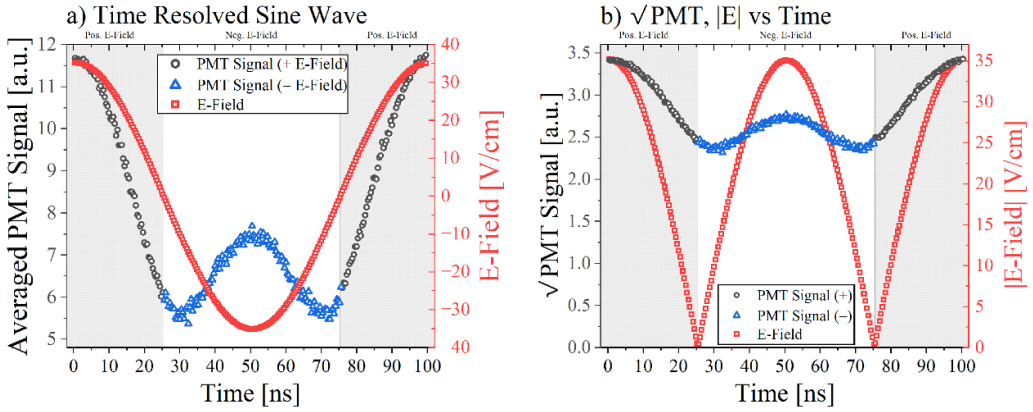

Figure 4. 400 ps time-resolved E-FISH data for a 10 MHz low voltage sine wave applied to the electrode assembly. The electrode gap distance is 3 mm. (a) Time-resolved E-Field and corresponding PMT signals. (b) $\sqrt{I_{\text{meas}}}$ plotted vs Time together with $|E|$ vs Time.

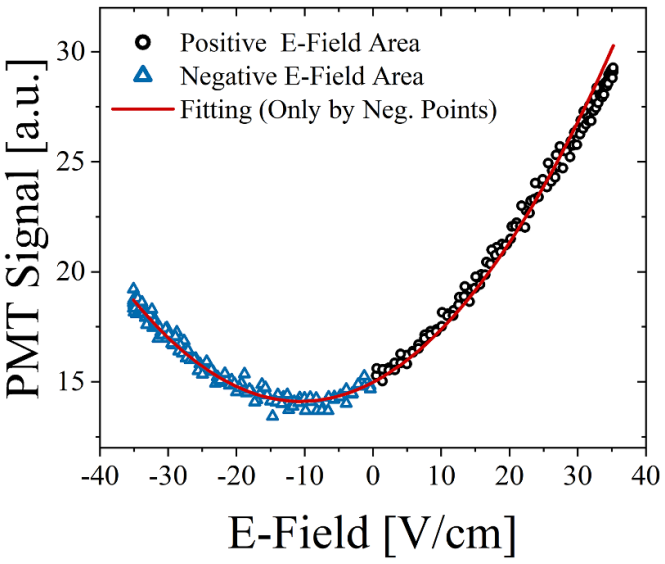

Figure 5. Measured PMT signal as a function of applied E-Field together with a parabola fit of the data. The laser pulse energy is 5 mJ.

where $\overline{\mathbf{E}}_{2\omega}^{\text{E-FISH}} = E_{2\omega}^{\text{E-FISH}} e^{i\phi_{\text{E-FISH}}}$. $E_{2\omega}^{\text{E-FISH}}$ is the magnitude of the electric field of the E-FISH signal with phase $\phi_{\text{E-FISH}}$. Similarly, $\overline{\mathbf{E}}_{2\omega}^{\text{LO}} = E_{2\omega}^{\text{LO}} e^{i\phi_{\text{LO}}}$. $E_{2\omega}^{\text{LO}}$ is the magnitude of the electric field of the coherent background signal with a phase ϕ_{LO}. To simplify the following expressions, we define the relative phase difference between the LO and E-FISH signals as $\phi = \phi_{\text{LO}} - \phi_{\text{E-FISH}}$ and define $\phi_{\text{E-FISH}}$ as 0. This means that equation (2) can be simplified as $\overline{\mathbf{E}}_{\text{total}} = E_{2\omega}^{\text{E-FISH}} + E_{2\omega}^{\text{LO}} e^{i\phi}$.

We can write the electric field from the E-FISH process as:

$$E_{2\omega}^{\text{E-FISH}} = |\overline{\mathbf{E}}_{2\omega}^{\text{E-FISH}}| \propto |\chi^{(3)} \overline{\mathbf{E}}_{\text{appl}} \overline{\mathbf{E}}_{\omega} \overline{\mathbf{E}}_{\omega}|, \tag{3}$$

where $\chi^{(3)}$ denotes the third-order nonlinear susceptibility of the gas (room air in the present case), whereas $\overline{\mathbf{E}}_{\omega}$ represents the complex notation of the electric field of the incident 1064 nm laser beam. The SHG electric field from the LO can be written as:

$$E_{2\omega}^{\text{LO}} = |\overline{\mathbf{E}}_{2\omega}^{\text{LO}}| \propto |\chi^{(2)} \overline{\mathbf{E}}_{\omega} \overline{\mathbf{E}}_{\omega}|, \tag{4}$$

where $\chi^{(2)}$ is the second-order nonlinear susceptibility of the dichroic mirror surface.

Inserting equation (2) into equation (1) yields:

$$I_{\text{meas}} \propto I_{2\omega}^{\text{LO}} + I_{2\omega}^{\text{E-FISH}} + 2E_{2\omega}^{\text{E-FISH}} E_{2\omega}^{\text{LO}} \cos(\phi), \tag{5}$$

where $I_{2\omega}^{\text{E-FISH}} = |\overline{\mathbf{E}}_{2\omega}^{\text{E-FISH}}|^2 = (E_{2\omega}^{\text{E-FISH}})^2$ and $I_{2\omega}^{\text{LO}} = |\overline{\mathbf{E}}_{2\omega}^{\text{LO}}|^2 = (E_{2\omega}^{\text{LO}})^2$ are the intensities of the E-FISH and LO signals, respectively.

Combining equations (3)–(4) into equation (5) yields:

$$I_{\text{meas}} \propto \beta |\overline{\mathbf{E}}_{\omega}|^4 + \alpha |\overline{\mathbf{E}}_{\text{appl}}|^2 |\overline{\mathbf{E}}_{\omega}|^4 + \gamma |\overline{\mathbf{E}}_{\text{appl}}| |\overline{\mathbf{E}}_{\omega}|^4 \cos(\phi) \tag{6}$$

where α and β are positive proportionality constants related to the efficiencies of the SHG and E-FISH processes, respectively. $\gamma = 2\sqrt{\alpha\beta}$.

The first term of equation (6) represents the intensity of the SHG signal emanating from the interaction of the incident laser beam with the dichroic mirror surface ($I_{2\omega}^{\text{LO}}$). The second term represents the intensity of the E-FISH process ($I_{2\omega}^{\text{E-FISH}}$). The third term finally is ascribed to the interference between the surface SHG and E-FISH signals. It is responsible for a decrease in the intensity of the measured signal with increasing applied electric field. Constructive interference occurs when $\phi = 0$, i.e. $\cos(\phi) = 1$. Conversely, destructive interference is achieved for $\phi = \pi$, i.e. $\cos(\phi) = -1$.

In equation (6)'s paradigm, when $\cos(\phi) < 0$, meaning $\frac{\pi}{2} < \phi < \frac{3\pi}{2}$, it is possible to observe a decrease in measured intensity I_{meas} with an increase in the magnitude of the applied electric field $|\overline{\mathbf{E}}_{\text{appl}}|$. When writing $Y = I_{\text{meas}}$ and $X = |\overline{\mathbf{E}}_{\text{appl}}|$, equation (6) can be identified as a quadratic function of $|\overline{\mathbf{E}}_{\text{appl}}|$:

$$Y = AX^2 + BX + C, \tag{7}$$

where $A = \alpha |\overline{\mathbf{E}}_{\omega}|^4$, $B = \gamma |\overline{\mathbf{E}}_{\omega}|^4 \cos(\phi)$, and $C = \beta |\overline{\mathbf{E}}_{\omega}|^4$ are proportionality constant non-dependent on $|\overline{\mathbf{E}}_{\text{appl}}|$. To validate

this interpretation of our measurements, we fitted the negative E-fields portion of the data displayed on figure 5 using equation (7). A great quality fit ($R^2 = 0.995$) was obtained and overlaid on top of the negative E-fields experimental results. When using coefficients *A*, *-B*, and *C* from equation (7) for positive E-field values ranging from 0 to 35 $\mathrm{V\,cm^{-1}}$, we obtained a curve showing an excellent agreement with the positive E-fields data (overall $R^2 = 0.991$). The fact that the quadratic fit somewhat overestimates experimental results for positive E-fields above ≈25 $\mathrm{V\,cm^{-1}}$ could be a hint of a slight saturation of the PMT for the corresponding intensity range. Nonetheless, the good match obtained suggests our experimental findings are consistent with an enhanced E-FISH homodyne detection passively achieved through the interference of the regular E-FISH signal with the SHG signal produced from a dichroic mirror in the beam path. It is important to note that 'active' homodyne E-FISH detection of gas-phase electric fields down to about 500 $\mathrm{V\,cm^{-1}}$ has been recently reported [41, 42], with also a demonstration of a sensitivity to the E-field polarity. In contrast, our setup realized it 'passively', in a single beam configuration achieving a detection limit better than 1 $\mathrm{V\,cm^{-1}}$. Furthermore, the sub-nanosecond temporal resolution (a capability not demonstrated by the aforementioned previous works) of our setup allows us to unravel the fundamental mechanisms of this interaction.

Our intuitive interpretation of the data relies on the fact that when the sign of the applied electric field $\mathbf{E}_{\mathrm{appl}}$ flips from positive to negative (or vice-versa), we get a π change in the phase difference ($\Delta\phi$) between the incident laser beam and the applied electric field: $\Delta\phi_2 = \Delta\phi_1 \pm \pi$. Where $\Delta\phi_1$ and $\Delta\phi_2$ are the phase differences before and after the sign flip (electric field reversal), respectively. As a result, $\cos(\Delta\phi_2) = -\cos(\Delta\phi_1)$. Such an interpretation, although appropriate in first order of approximation, does not account for the wave nature of the incident 1064 nm laser beam featuring a frequency about 2.82×10^{14} Hz. This means that within a single 30 ps laser pulse, while $\mathbf{E}_{\mathrm{appl}}$ is constant, the electric field of the incident light flips about 1.69×10^4 times (two sign flips per time period).

In the following, we now extend the previous model to account for the temporal evolution of the different electromagnetic waves at play. Assuming the electric field of the incident laser beam could be written as a 30 ps Gaussian envelope electromagnetic wave featuring a 1064 nm wavelength (≈ 3.55 fs time period), we get:

$$\mathbf{E}_{\omega} = E_{0,\omega}\, g\,(t)\, \cos\left(\omega_0 t\right), \tag{8}$$

where $E_{0,\omega}$ is the amplitude of the laser electric field, $g(t) = \mathrm{e}^{-4\ln 2\,(\frac{t}{\tau_p})^2}$ is the 30 ps Gaussian temporal envelope ($\tau_p = 30$ ps), and $\omega_0 = 2\pi\,\frac{c}{\lambda_0} \approx 1.77 \times 10^{15}$ rad $\mathrm{s^{-1}}$ is the angular frequency of the incident laser for $\lambda_0 = 1064$ nm. Note that τ_p corresponds to the FWHM of the incident laser beam electric field temporal profile. Consequently, it is equivalent to the full width at quarter maximum (FWQM) for the temporal profile of the incident laser beam intensity.

Similarly, the 10 MHz applied AC electric field can be written as:

$$\mathbf{E}_{\mathrm{appl}} = E_{0,AC}\, \cos\left(2\pi\, f_{\mathrm{AC}}\, t + \phi_{\mathrm{AC}}\right), \tag{9}$$

where $E_{0,AC} = 35$ $\mathrm{V\,cm^{-1}}$, is the amplitude of the applied AC electric field and $f_{\mathrm{AC}} = 10$ MHz is the frequency of the AC wave. ϕ_{AC} is the phase of the applied AC electric field.

Substituting equations (8) and (9) into equations (1)–(4) yields:

$$\begin{aligned} I_{\mathrm{meas}} \propto |\alpha E_{0,\mathrm{AC}} \cos\left(2\pi f_{\mathrm{AC}} t + \phi_{\mathrm{AC}}\right) E_{0,\omega}^2 g^2\,(t) \cos^2\left(\omega_0 t\right) \\ + \beta E_{0,\omega}^2 g^2\,(t) \cos^2\left(\omega_0 t\right) \mathrm{e}^{\mathrm{i}\phi}|^2. \end{aligned} \tag{10}$$

Equation (10) can be simplified into:

$$I_{\mathrm{meas}}\,(t) \propto |\alpha F_1\,(t) + \beta F_2\,(t)\, \mathrm{e}^{\mathrm{i}\phi}|^2, \tag{11}$$

where $F_1(t) = E_{0,\mathrm{AC}} \cos(2\pi f_{\mathrm{AC}} t + \phi_{\mathrm{AC}}) E_{0,\omega}^2 g^2(t) \cos^2(\omega_0 t)$ and $F_2(t) = E_{0,\omega}^2 g^2(t) \cos^2(\omega_0 t)$.

Equation (11) can be further simplified into:

$$I_{\mathrm{meas}}\,(t) \propto |F_1\,(t) + \eta F_2\,(t)\, \mathrm{e}^{\mathrm{i}\phi}|^2, \tag{12}$$

where $\eta = \frac{\beta}{\alpha}$. η and ϕ are the only two optimization parameters in our model.

Now considering a single laser pulse, the time-integrated signal $S(\mathbf{E}_{\mathrm{appl}})$ measured by the PMT can therefore be written as:

$$S\left(\mathbf{E}_{\mathrm{appl}}\right) = \int_{-\tau_p}^{\tau_p} I_{\mathrm{meas}}\,(t)\,\mathrm{d}t \propto \int_{-\tau_p}^{\tau_p} |F_1\,(t) + \eta F_2\,(t)\, \mathrm{e}^{\mathrm{i}\phi}|^2 \mathrm{d}t. \tag{13}$$

Based on our model, we should be able to use equation (13) for different values of $\mathbf{E}_{\mathrm{appl}}$ and essentially build a Matlab-based fit matching experimental data presented in figures 5 and 4(b). For this purpose, the Matlab least-squares nonlinear curve fitting tool lsqcurvefit is deployed. Figure 6 depicts the results of our model when compared to experimental results in terms of time-integrated PMT signal vs applied E-field. In figure 6(a), we show that our Matlab simulations are able to capture accurately the intensity offset and asymmetry discussed previously. Furthermore, figure 6(b) demonstrates that when compared with the applied AC wave, the temporal dynamics are also fully reproduced.

The excellent agreement obtained from figure 6 allows us to dig more into the details of the homodyne E-FISH process when selecting a few notable points in time from the AC wave dynamics. For instance, figure 7 focuses on characterizing the interaction process at the peak applied E-field: for $\mathbf{E}_{\mathrm{appl}} = +35$ $\mathrm{V\,cm^{-1}}$ ($t = 0$ ns or $t = 100$ ns). Note that the peak homodyne signal for the AC wave is obtained for the peak applied E-field. Figures 7(a)–(e) display the temporal evolution of the incident 30 ps laser electric field, its intensity, the applied AC electric field, the electric field of the generated 'pure' E-FISH signal, and the intensity of the measured homodyne signal, respectively.

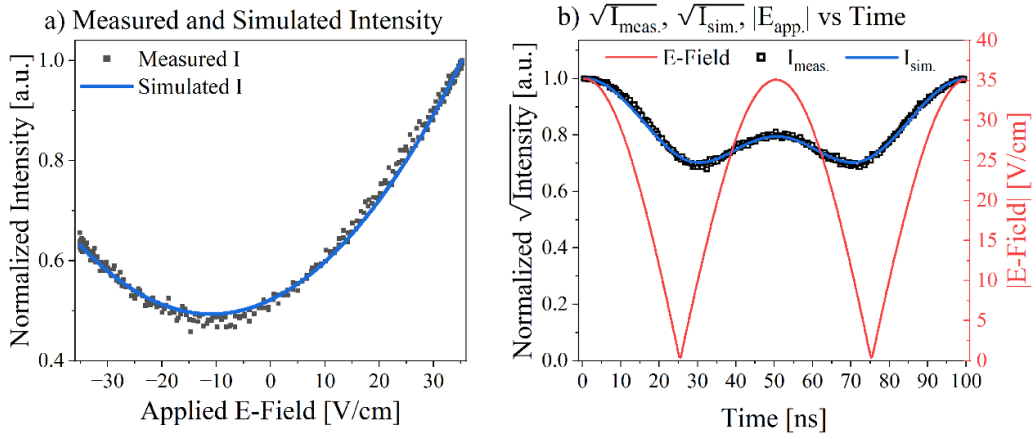

Figure 6. Comparison between simulations and experimental results. (a) Time-integrated PMT signal vs Applied E-Field. (b) Inferred $\sqrt{\text{PMT}}$, $|E|$ vs Time.

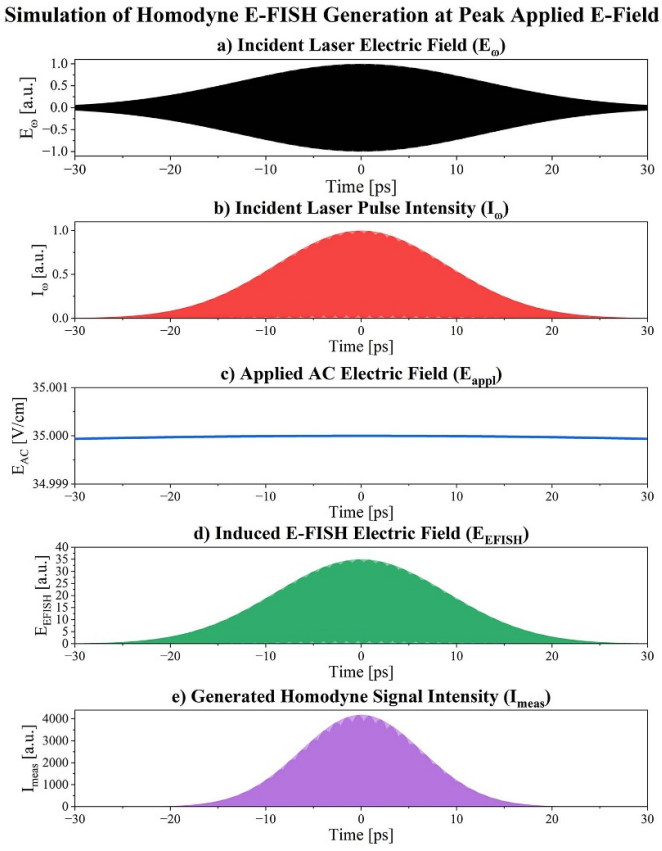

Figure 7. Single laser pulse simulations for the case where the AC electric field is maximum ($\phi_{\text{AC}} = 0$), generating maximum E_{EFISH} and I_{meas}. (a) Incident laser E-field. (b) Incident laser intensity. (c) Applied AC E-field. (d) Induced E-FISH E-field. (e) Generated homodyne signal intensity.

Figure 8 showcases the very same calculations but this time for $\mathbf{E}_{\text{appl}} = 0, -10\ \text{V cm}^{-1}$, respectively. While $\mathbf{E}_{\text{appl}} = 0\ \text{V cm}^{-1}$ is obtained at $t \approx 26$ ns, $\mathbf{E}_{\text{appl}} = -10\ \text{V cm}^{-1}$, which corresponds to the point in time for which the minimum homodyne signal is measured, is obtained at $t \approx 30$ ns. Comparing figures 7 and 8, on one hand we observe that as expected, a non-null homodyne E-FISH signal is generated for $\mathbf{E}_{\text{appl}} = 0\ \text{V cm}^{-1}$. The signal depicted in figure 8(e) corresponds in fact to the intensity of the signal from the LO. The latter signal is comparable in magnitude but a bit stronger than the minimum measured signal, which occurred at $\mathbf{E}_{\text{appl}} = -10\ \text{V cm}^{-1}$ (see figure 8(j)). On the other hand, the magnitude of the signal measured for the peak applied field is predicted to be a factor ≈ 2 stronger (see figure 7(e)), which is very consistent with our experimental measurements. Very interestingly, it is observed that from both figures 7 and 8, our model predicts a systematic 'temporal compression' of the incident laser pulse by the E-FISH process. The FWQM of the generated homodyne signal intensity temporal profiles are about 20 to 22 ps, instead of 30 ps. Such a phenomenon is typical for SHG processes [43].

The results presented in this manuscript represent a significant milestone in enhancing the sensitivity of the E-FISH diagnostic. While we are aware of recent similar advancements employing single beam homodyne enhancement (where the interference term in equations (5) and (6) completely dominates the sum) to achieve improved E-FISH sensitivity by the group at Polytechnique Montréal [44], further improvements in the detection limit remain possible. Potential avenues include: (1) adopting an all-reflective optics approach in the collection part of the setup; (2) employing a gated photon-counting photomultiplier tube as the endpoint detector; (3) developing an 'active' homodyne experimental setup allowing for a precise adjustment of the phase difference and LO intensity, to operate within different regimes of the interference effects; and (4) utilizing femtosecond MHz repetition rate lasers to address scenarios requiring large numbers of laser shots ($>10^4$), particularly in plasma applications. Notably, many of these strategies have been successfully implemented by Dadap *et al* [37] but for the purpose of surface electric field measurements. Our findings demonstrate that this approach is well-suited for gas phase electric field

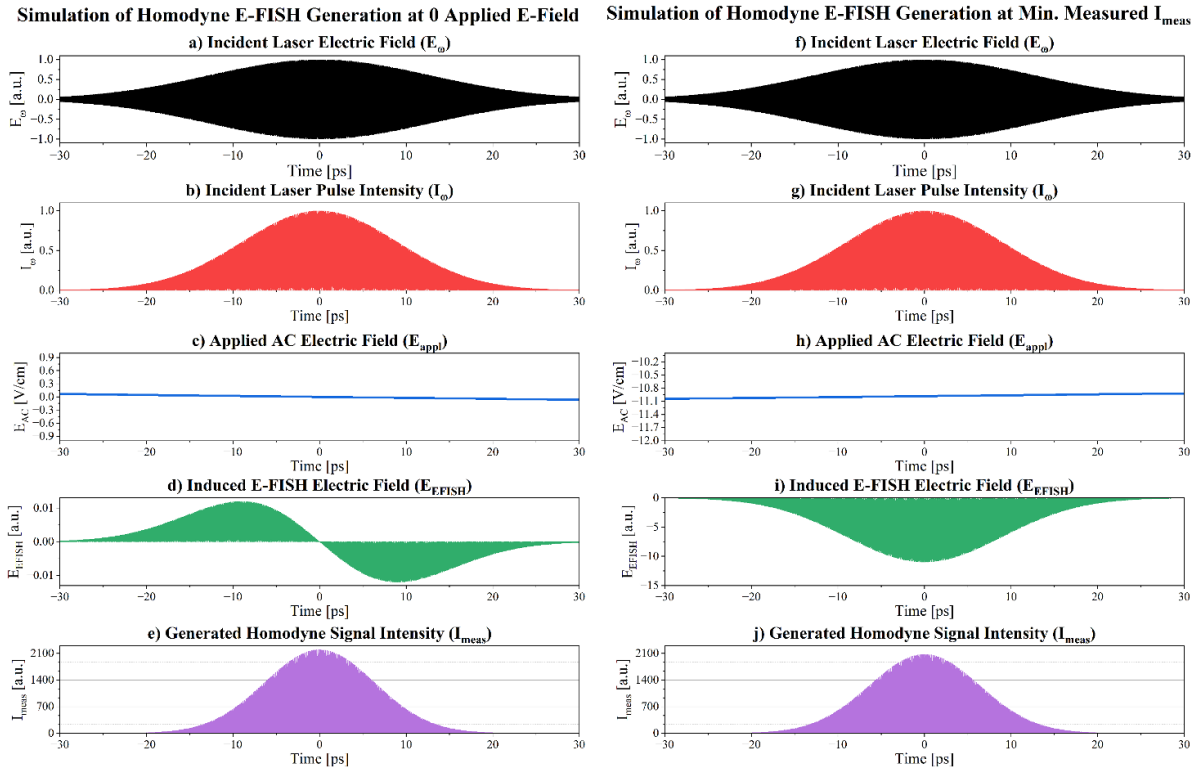

Figure 8. Single laser pulse simulations for the cases where the applied E-field is null (left) and $-10\ \mathrm{V\,cm^{-1}}$ (right). (a) Incident laser E-field. (b) Incident laser intensity. (c) Applied E-field for $\phi_{\mathrm{AC}} = \frac{\pi}{2}$. (d) Induced E-FISH E-field for $\phi_{\mathrm{AC}} = \frac{\pi}{2}$. (e) Generated homodyne signal intensity for $\phi_{\mathrm{AC}} = \frac{\pi}{2}$. (f) Incident laser E-field. (g) Incident laser intensity. (h) Applied E-field for $\phi_{\mathrm{AC}} = \frac{3\pi}{5}$. (i) Induced E-FISH E-field for $\phi_{\mathrm{AC}} = \frac{3\pi}{5}$. (j) Generated homodyne signal intensity for $\phi_{\mathrm{AC}} = \frac{3\pi}{5}$.

measurements while preserving the sub-nanosecond temporal resolution.

Everything considered, we demonstrated the potential to utilize what might be considered an unwanted stray signal. However, in plasma setups with chambers containing optical windows, additional stray light signals could be generated. These effects could be mitigated by either decreasing the beam intensity at windows or directly incorporating optics within the test chamber, where feasible, to isolate the second harmonic E-FISH beam from the fundamental beam before it reaches the chamber windows.

5. Conclusion

In conclusion, we demonstrated DC and AC E-FISH-based electric field measurements to magnitudes lower than 1 $\mathrm{V\,cm^{-1}}$ for Laplacian field configurations in room air. The detection limit of our system was estimated to be approximately 0.3–0.5 $\mathrm{V\,cm^{-1}}$. A 400 ps temporal resolution was achieved for the AC measurements. Sensitivity to the phase of the electric field is achieved through homodyne detection arising from the unexpected interference of the E-FISH signal with stray SHG signal from the surface of a dichroic mirror in the beam path. The high-sensitivity of our experimental setup is attributed to several key factors: (1) homodyne detection; (2) use of a very sensitive PMT under high gain conditions; (3) meticulous optimization of the E-FISH collection leg optics and alignment; (4) precise adjustment of the electrode length for our incident laser beam focusing conditions; and (5) a high-quality spatial profile of the incident laser beam. Our experimental results were found to be in excellent agreement with analytical simulations of the E-FISH signal for a homodyne process. Interestingly, the analytical simulations of the E-FISH signal predicted that the E-FISH process, similarly to SHG processes should result in a temporal compression of the incident laser pulse. This work opens up new opportunities for improved single-shot and 2D measurements under high-pressure conditions. Additionally, we expect the homodyne approach to also improve the performance of the E-FISH diagnostic under very low pressure conditions (0.1–1 Pa), for which the 'standard' E-FISH approach is not well-suited because of the N^2 dependence of the signal on the gas density N. Between 1 atm ($\approx 10^5$ Pa) and 1 Pa, because N decreases by 5 orders of magnitude, the E-FISH signal is therefore expected to decrease by 10 orders of magnitude (when not accounting for homodyne enhancement). Finally, we plan to leverage the newly gained sensitivity for precise characterization of electric field reversals in a variety of discharge geometries.

Data availability statement

All data that support the findings of this study are included within the article (and any supplementary files).

Acknowledgments

The support of the U S National Science Foundation under award PHY 2308946 is gratefully acknowledged. We also acknowledge the financial support of the College of Science and Engineering and the Department of Mechanical Engineering of the University of Minnesota, Twin Cities. We would like to thank Dr Jérémy Rouxel (Argonne National Laboratory) as well as Thomas Cameron (University of Minnesota) for fruitful discussions.

ORCID iDs

Grayson LaCombe https://orcid.org/0009-0005-1505-9683
Jianan Wang https://orcid.org/0000-0003-1344-237X
Kraig Frederickson https://orcid.org/0009-0007-2510-6126
Marien Simeni Simeni https://orcid.org/0000-0002-2241-5739

References

[1] Adamovich I *et al* 2022 The 2022 plasma roadmap: low temperature plasma science and technology *J. Phys. D: Appl. Phys.* **55** 373001
[2] Lieberman M A and Lichtenberg A J 1994 Principles of plasma discharges and materials processing *MRS Bull.* **30** 899–901
[3] Raizer Y P and Allen J E 1997 *Gas Discharge Physics* vol 2 (Springer)
[4] Bruggeman P J, Iza F and Brandenburg R 2017 Foundations of atmospheric pressure non-equilibrium plasmas *Plasma Sources Sci. Technol.* **26** 123002
[5] Simeni M S, Goldberg B, Gulko I, Frederickson K and Adamovich I V 2017 Sub-nanosecond resolution electric field measurements during ns pulse breakdown in ambient air *J. Phys. D: Appl. Phys.* **51** 01LT01
[6] Dogariu A, Goldberg B M, O'Byrne S and Miles R B 2017 Species-independent femtosecond localized electric field measurement *Phys. Rev. Appl.* **7** 024024
[7] Simeni M S, Tang Y, Hung Y-C, Eckert Z, Frederickson K and Adamovich I V 2018 Electric field in Ns pulse and AC electric discharges in a hydrogen diffusion flame *Combust. Flame* **197** 254–64
[8] Tang Y, Simeni Simeni M, Yao Q and Adamovich I V 2022 Non-premixed counterflow methane flames in DC/AC/NS electric fields *Combust. Flame* **240** 112051
[9] Retter J E and Elliott G S 2019 On the possibility of simultaneous temperature, species and electric field measurements by coupled hybrid fs/ps CARS and EFISHG *Appl. Opt.* **58** 2557–66
[10] Goldberg B M, Reuter S, Dogariu A and Miles R B 2019 1D time evolving electric field profile measurements with sub-ns resolution using the E-FISH method *Opt. Lett.* **44** 3853–6
[11] Orr K, Tang Y, Simeni Simeni M, Van Den Bekerom D and Adamovich I V 2020 Measurements of electric field in an atmospheric pressure helium plasma jet by the E-FISH method *Plasma Sources Sci. Technol.* **29** 035019
[12] Lepikhin N D, Luggenhölscher D and Czarnetzki U 2020 Electric field measurements in a He: N_2 nanosecond pulsed discharge with sub-ns time resolution *J. Phys. D: Appl. Phys.* **54** 055201
[13] Goldberg B M, Loon Chng T, Dogariu A and Miles R B 2018 Electric field measurements in a near atmospheric pressure nanosecond pulse discharge with picosecond electric field induced second harmonic generation *Appl. Phys. Lett.* **112** 064102
[14] Loon Chng T, Brisset A, Jeanney P, Starikovskaia S M, Adamovich I V and Pierre T 2019 Electric field evolution in a diffuse ionization wave nanosecond pulse discharge in atmospheric pressure air *Plasma Sources Sci. Technol.* **28** 09LT02
[15] Tat L C, Orel I S, Starikovskaia S M and Adamovich. I V 2019 Electric field induced second harmonic (E-FISH) generation for characterization of fast ionization wave discharges at moderate and low pressures *Plasma Sources Sci. Technol.* **28** 045004
[16] Zhu Y, Chen X, Yun W, Hao J, Xiaoguang M, Pengfei L and Tardiveau P 2021 Simulation of ionization-wave discharges: a direct comparison between the fluid model and E-FISH measurements *Plasma Sources Sci. Technol.* **30** 075025
[17] Chen T Y, Mao X, Zhong H, Lin Y, Liu N, Goldberg B M, Yiguang J and Kolemen E 2023 Impact of CH_4 addition on the electron properties and electric field dynamics in a Ar nanosecond-pulsed dielectric barrier discharge *Plasma Sources Sci. Technol.* **31** 125013
[18] Adamovich I V, Butterworth T, Orriere T, Pai D Z, Lacoste D A and Suk Cha M 2020 Nanosecond second harmonic generation for electric field measurements with temporal resolution shorter than laser pulse duration *J. Phys. D: Appl. Phys.* **53** 145201
[19] Cui Y, Zhuang C and Zeng R 2019 Electric field measurements under DC corona discharges in ambient air by electric field induced second harmonic generation *Appl. Phys. Lett.* **115** 244101
[20] Strobel L R, Martell B C, Morozov A, Dogariu A and Guerra-Garcia C 2022 Electric field measurements of DC-driven positive streamer coronas using the E-FISH method *Appl. Phys. Lett.* **121** 114102
[21] Elliott S, Dogariu A, Coates C and Leonov S B 2022 Electric charge build-up and dissipation at pulsed streamer corona by EFISH and probe measurements *Plasma Sources Sci. Technol.* **31** 124003
[22] Simeni M S, Tang Y, Frederickson K and Adamovich. I V 2018 Electric field distribution in a surface plasma flow actuator powered by NS discharge pulse trains *Plasma Sources Sci. Technol.* **27** 104001
[23] Huang B, Zhang C, Adamovich I, Akishev Y and Shao T 2020 Surface ionization wave propagation in the nanosecond pulsed surface dielectric barrier discharge: the influence of dielectric material and pulse repetition rate *Plasma Sources Sci. Technol.* **29** 044001
[24] Chng T L, Starikovskaia S M and Schanne-Klein M-C 2020 Electric field measurements in plasmas: how focusing strongly distorts the E-FISH signal *Plasma Sources Sci. Technol.* **29** 125002
[25] Chen T Y, Liu N, Zhong H, Mao X, Goldberg B M, Kliewer C J, Kolemen E and Yiguang J 2024 Quantitative

time-resolved diagnostics of electric field dynamics during individual plasma breakdown events using burst laser pulse electric field induced second harmonic generation *Appl. Phys. Lett.* **125** 054102
[26] Raskar S, Orr K, Adamovich I V, Chng T L and Starikovskaia S M 2022 Spatially enhanced electric field induced second harmonic ((SEEFISH) generation for measurements of electric field distributions in high-pressure plasmas *Plasma Sources Sci. Technol.* **31** 085002
[27] Vorenkamp M, Steinmetz S A, Chen T Y, Yiguang J and Kliewer C J 2023 Suppression of coherent interference to electric-field-induced second-harmonic (E-FISH) signals for the measurement of electric field in mesoscale confined geometries *Opt. Lett.* **48** 1930–3
[28] Sogame M, Nakamura S, Sato M, Fujii T and Kumada A 2024 Adequate laser focusing and signal acquisition conditions for 3D measurement of electric-field distribution by the E-FISH method *Plasma Sources Sci. Technol.* **33** 055001
[29] Simeni M S, Goldberg B M, Zhang C, Frederickson K, Lempert W R and Adamovich I V 2017 Electric field measurements in a nanosecond pulse discharge in atmospheric air *J. Phys. D: Appl. Phys.* **50** 184002
[30] Raskar S, Orr K, Yang X and Adamovich I V 2022 Electric field distribution in a non-self-sustained RF discharge with ionization generated by Ns discharge pulses *Plasma Sources Sci. Technol.* **31** 124001
[31] Abuyazid N H, Üner N B, Peyres S M and Mohan Sankaran R 2023 Charge decay in the spatial afterglow of plasmas and its impact on diffusion regimes *Nat. Commun.* **14** 6776
[32] Ono T, Kortshagen U R and Hogan C J 2021 Material-dependent submicrometer particle trapping in capacitively-coupled plasma sheaths in an intermediate collision regime *Plasma Sources Sci. Technol.* **30** 095014
[33] Mazouffre S 2012 Laser-induced fluorescence diagnostics of the cross-field discharge of Hall thrusters *Plasma Sources Sci. Technol.* **22** 013001
[34] Charles C 2007 A review of recent laboratory double layer experiments *Plasma Sources Sci. Technol.* **16** R1
[35] Burrell K H *et al* 1994 Role of the radial electric field in the transition from L (low) mode to H (high) mode to VH (very high) mode in the DIII D tokamak *Phys. Plasmas* **1** 1536–44
[36] Aanesland A, Bredin J and Chabert P 2014 A review on ion–ion plasmas created in weakly magnetized electronegative plasmas *Plasma Sources Sci. Technol.* **23** 044003
[37] Dadap J I, Shan J, Weling A S, Misewich J A and Heinz T F 1999 Homodyne detection of second-harmonic generation as a probe of electric fields *Appl. Phys. B: Lasers Opt.* **68** 333–41
[38] Chang R K, Ducuing J and Bloembergen N 1965 Relative phase measurement between fundamental and second-harmonic light *Phys. Rev. Lett.* **15** 6
[39] Stolle R, Marowsky G, Schwarzberg E and Berkovic G 1996 Phase measurements in nonlinear optics *Appl. Phys.* B **63** 491–8
[40] Mrkvičková M, Kuthanová L, Bílek P, Obrusník A, Navrátil Z, Dvořák P, Adamovich I, Šimek M and Hoder T 2023 Electric field in APTD in nitrogen determined by EFISH, FNS/SPS ratio, α-fitting and electrical equivalent circuit model *Plasma Sources Sci. Technol.* **32** 065009
[41] Hogue J, Cusson P, Meunier M, Seletskiy D V and Reuter S 2023 Sensitive detection of electric field-induced second harmonic signals *Opt. Lett.* **48** 4601–4
[42] Billeau J-B, Cusson P, Dogariu A, Morozov A, Seletskiy D V and Reuter S 2024 Coherent homodyne detection for amplified cross-beam electric-field induced second harmonic *Appl. Opt.* **63** 5203–7
[43] Kim D-W, Xiao G-Y and Guo-Bin M 1997 Temporal properties of the second-harmonic generation of a short pulse *Appl. Opt.* **36** 6788–93
[44] Billeau J-B, Cusson P, Seletskiy D and Reuter S 2025 Optical inline interferometer for enhanced low-field detection via electric-field induced second harmonic generation *Plasma Sources Sci. Technol.* (https://doi.org/10.1088/13616595/adad13)